ARTICLE

Hybrid Theranostic Microbubbles for Ultrasound/Photoacoustic Imaging Guided Starvation/Low-Temperature Photothermal/Hypoxia-Activated Synergistic Cancer Therapy

ROSReceived 00th January 20xx,
Accepted 00th January 20xx

DOI: 10.1039/x0xx00000x

Feng Tian,[a] Xingjian Zhong, [a] JunKai Zhao,[b] Yutian Gu, [a] Yadi Fan, [a] Fan Shi, [a] Yu Zhang,[c] Youhua Tan,[a] Wen Chen,[d] Changqing Yi, *[b] and Mo Yang *[a]

Constructing a theranostic agent for high-contrast multimodality imaging-guided synergistic therapy with long-term tumor retention and minimum systemic side effects still remains a major challenge. Herein, a hybrid microbubble-based theranostic platform was developed for dual-modality ultrasound (US) and enhanced photoacoustic (PA) imaging-guided synergistic tumor therapy by combining starvation therapy, low-temperature photothermal therapy (PTT), and hypoxia-activated therapy, based on polydopamine (PDA) doped poly (vinyl alcohol) microbubbles loaded with glucose oxidase (GOx) (PDA–PVAMBs@GOx) and hypoxia-activated prodrug (HAP) tirapazamine (TPZ). For dual-modality US/enhanced PA imaging, PDA–PVAMBs provided 6.5-fold amplified PA signal relative to freely dispersed PDA nanoparticles (PDA NPs). For synergistic cancer therapy, oxygen (O_2) carried by PDA–PVAMBs@GOx was first released to promote starvation therapy by loaded GOx. Then moderate near-infrared (NIR) laser irradiation triggered PTT and improved enzymatic activity of GOx with its optimal activity around 47 ℃. Subsequently, GOx-mediated tumor starvation depleted O_2 and exacerbated hypoxia environment, thereby activating the toxicity of TPZ in the tumor site. Through dual-modality US/PA imaging monitoring, PDA–PVAMBs@GOx with long-term retention (~7 days) combined with PTT and TPZ significantly inhibited the growth of solid tumors with minimum systemic side effects, which might be a powerful tool for effective tumor treatment.

1. Introduction

Combinational cancer therapy is to achieve better therapeutic effects by combining different treatment methods. An ideal combinational therapy should not only improve the efficacy and reduce side effects, but also show complementary features to achieve a win-win outcome.[1-3] As an emerging tool in cancer therapy, starvation therapy has shown great potential by targeting its high nutrient consumption and abnormal metabolism.[4-5] In recent studies, glucose oxidase (GOx) has attracted much interest as a therapeutic agent for starvation therapy due to its biocatalytic properties, which can effectively catalyze the oxidation of glucose into hydrogen peroxide (H_2O_2) and gluconic acid in the presence of oxygen (O_2).[6-13] Such a catalytic reaction can significantly lower glucose and O_2 level in localized tumor microenvironments, creating the starvation effect for cancer treatment. Moreover, the in-situ generated H_2O_2, a type of reactive oxygen species (ROS), can also lead to cellular apoptosis as a supplement.[14] However, recent studies also indicate that the therapeutic effect of GOx-mediated monotherapy is rather limited by the insufficient O_2 level, therefore additional O_2 supply and synergistically combining with other therapeutic methods are needed to achieve a higher efficiency. [6,7,15]

Among various other therapy approaches, hypoxia-activated prodrugs (HAPs) are promising candidates which are intrinsically non-toxic and become toxic in the hypoxia environment.[16,17] Taking advantage of tumoral hypoxia generated by starvation therapy, the addition of HAPs can achieve sequential and synergistic tumor therapeutic effects.[8,10,11] Besides, photothermal therapy (PTT), a powerful technique with minimal invasiveness, shows potential as a complement to enhance the overall therapeutic outcomes.[9,18] Triggered by near-infrared (NIR) light, photothermal agents produce local hyperthermia by converting optical energy to heat and kill tumor cells.[19,20] However, the inevitable hyperthermia and overdose of photothermal agents may cause undesired damage to surrounding normal tissues.[9,18,21] Therefore, combining with GOx-based starvation therapy, such side effects can be avoided by low-temperature PTT (< 50 ℃)

[a] Department of Biomedical Engineering, The Hong Kong Polytechnic University, Hong Kong S. A. R., China
[b] Key Laboratory of Sensing Technology and Biomedical Instruments (Guangdong Province), School of Biomedical Engineering, Sun Yat-Sen University, Guangzhou, 510006, P. R. China.
[c] Department of Mechanical and Automotive Engineering, Royal Melbourne Institute of Technology University, Melbourne, Victoria 3000, Australia
[d] Department of Electronic and Information Engineering, The Hong Kong Polytechnic University, Hong Kong S. A. R., China
Electronic Supplementary Information (ESI) available: [details of any supplementary information available. See DOI: 10.1039/x0xx00000x

based on lowered NIR laser power and PTT agents dose.[9,18] Moreover, the elevated temperature improves the enzymatic activities of the GOx, leading to a back-feeding effect.[18, 22] As far as we know, there is a lack of platforms that can combine therapeutic approaches of starvation, HAPs, and PTT to reach synergistic effects. It is expected that a higher synthetic therapeutic efficacy with less side effects will be achieved with the combination of the above three therapeutic approaches.

With the development of precision medicine, therapeutic agents integrated with multimodality imaging capability are strongly needed for accurate and visualized high-quality imaging-guided treatment.[23-25] The combination of ultrasound (US) and photoacoustic (PA) imaging could be an excellent candidate for dual-mode imaging. Polymeric microbubbles (MBs) are stable agents for US contrast and the cavity in MBs can also carry O_2 for potential O_2-dependent theratpy.[26,27] The further loading PA imaging contrast agents on MBs may establish a single platform for both US and PA imaging contrast. PTT agents intrinsically serve as photoacoustic (PA) imaging contrast agents based on the light-heat-ultrasonic oscillation effect.[28] Hence, the integration of GOx, polymeric microbubbles, and PTT agents also as PA imaging contrast agents could synergistically achieve the US/PA imaging guided starvation, photothermal, and hypoxia-activated therapy.

In this study, we developed novel theranostic hybrid MBs based on GOx-loaded polydopamine doped poly (vinyl alcohol) MBs (PDA–PVAMBs@GOx) together with hypoxia-activated drug tirapazamine (TPZ) (PDA–PVAMBs@GOx–TPZ) for dual-modality US/enhanced PA imaging-guided synergistic therapy by combination of starvation therapy, low-temperature PTT, and hypoxia-activated therapy (Scheme 1). Here, PVA was used to fabricate polymeric MBs while PDA not only provided PA imaging contrast and PTT, but also served as an interfacial layer to load GOx.[29-31] Importantly, PA contrast of the PDA was significantly amplified and stabilized by PVAMBs by 6.5 fold due to the agglomeration-induced local temperature enhancement, MBs resonance, and in-situ nanobubbles generation for long-term US/PA monitoring. [32-34] For synergistic therapy, O_2 in the cavity of MBs was first released to the surrounding hypoxia tumor microenvironment, supporting the depletion of glucose and generation of H_2O_2 by GOx reaction. Under moderate NIR irradiation, PDA generated PTT and enhanced the enzymatic activity of GOx. Additionally, the subsequently generated hypoxia during GOx reaction triggered the toxicity of TPZ, leading to a synergistic therapeutic effect. *In vivo* dual-modality US/PA imaging showed a long retention time of PDA–PVAMBs@GOx in the tumor after the intratumoral injection up to 7 days due to their micrometer size. Both *in vitro* and *in vivo* studies demonstrated that the combinational therapy with PDA–PVAMBs@GOx–TPZ could significantly inhibit the growth of solid tumors under NIR irradiation based on the triple synergistic therapy with minimum systemic side effects.

2. Materials and Methods

2.1. Materials Measurement

Poly (vinyl alcohol) (PVA) with a weight-average molecular weight of 89,000-98,000 g/mol and 99+% hydrolyzed degree, dopamine hydrochloride, rhodamine B isothiocyanate (RBITC), sodium metaperiodate ($NaIO_4$), were purchased from Sigma Aldrich, USA. LIVE/DEAD™ Cell Imaging Kit (Invitrogen™) and Image-iT™ Hypoxia Reagent (Invitrogen™) were purchased from ThermoFisher Scientific, USA. H_2O_2 Assay Kit and BCA Protein Assay Kit were purchased from Solarbio, China. Tirapazamine was purchased from Tokyo Chemical Industry Co., Japan. All other reagents and solvents were provided by Sinopharm Chemical Reagent Co., Ltd. All reagents and chemicals were purchased commercially and without further purification if not otherwise mentioned.

2.2. Measurement

An Ultrospec 2100 Pro spectrophotometer (Amersham Biosciences) was utilized to measure the UV–Vis–NIR extinction of PDA–PVAMBs. Zetasizer Nano ZS (Malvern Instruments,

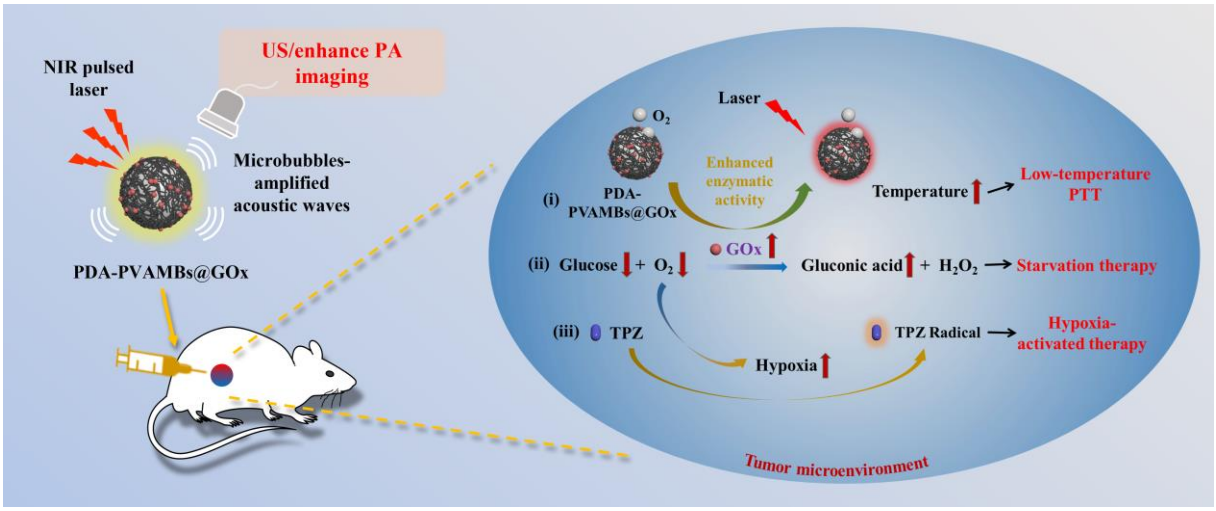

Scheme 1. Schematic illustration of PDA–PVAMBs@GOx–TPZ platform for dual-modality US/enhanced PA imaging-guided synergistic starvation, photothermal and hypoxia-activated therapy.

Malvern, UK) was utilized for the measurement of zeta potential and hydrodynamic size. A Leica TCS SPE Confocal Microscope was utilized for observation of RBITC stained PDA–PVAMBs. A Nikon Eclipse Ti2-E Live-cell Fluorescence Imaging System was utilized for the imaging of cells and tissue slides. A JEOL JSM 6335F Field emission scanning electron microscope (FESEM) (Tokyo, Japan) was utilized for the observation of the morphology of MBs. VEVO LAZR instrument from FUJIFILM VisualSonics (Amsterdam, NL) operating with an LZ250 transducer was utilized for US and PA imaging. The 808 nm NIR laser (CNI, China) was used for the *in vitro* and *in vivo* PTT.

2.3. Preparation of PDA–PVAMBs@GOx

PDA doped PVAMBs were firstly prepared using a one-pot synthesis method by doping PDA during the process of PVAMBs preparation.[35] Briefly, 1 g PVA was added in 50 mL deionized water (18.2 MΩ.cm) at 80 ℃ in a closed chamber filled with oxygen. After the complete dissolution, $NaIO_4$ was mixed and the solution was kept stirring at 500 rpm for 1h. Then 500 mg of dopamine hydrochloride was mixed to form PVA-dopamine complex through hydrogen bond and the mixture was intensively homogenized at 8000 rpm at 25 ℃ for 3 h using an Ultra-Turrax homogenizer. Oxygen was encapsulated in the shell with a PDA–PVA interfacial layer and the formed MBs would float to the surface of water. After several times of washing with a separating funnel, aqueous dispersion of PDA–PVAMBs was acquired with oxygen loading inside the internal microbubble core. To quantify the weight of PDA–PVAMBs, the prepared PDA–PVAMBs were concentrated and lyophilized. For GOx modification, 10^8 counts/mL PDA–PVAMBs were dispersed in 5 mL Tris buffer (10 mM, pH 8.0) and mixed with 5 mg GOx, following by shaking overnight. After the modification of GOx, PDA–PVAMBs@GOx floated to the liquid surface, which were then washed 3 times to remove the extra GOx. BCA Protein Assay Kit was used to measure the concentration of unbound GOx for the calculation of loading efficiency of GOx.

2.4 *In vitro* photothermal study

To evaluate the photothermal conversion performance of PDA–PVAMBs, an 808 nm laser with a power density of 1 W/cm^2 was used to irradiate 1 mL PDA–PVAMBs with different concentrations from 0 to 0.5×10^8 counts/mL for 5 min. To evaluate the effect of laser power on the temperature increase, PDA–PVAMBs solution with a fixed concentration of 0.5×10^8 counts/mL was irradiated under an 808 nm laser for 5 min with a power density of 0, 0.25, 0.5, and 1 W/cm^2, respectively. Finally, for the study of photothermal stability, PDA–PVAMBs were first exposed to an 808 nm laser with a power density of 1 W/cm^2 for 5 min, then cooled down to room temperature. This process continued for 5 cycles. To evaluate the difference of photothermal conversion between PDA–PVAMBs and PDA–PVAMBs@GOx, 0.5×10^8 counts/mL of PDA–PVAMBs@GOx were irradiated with 808 nm laser at 1 W/cm^2 power density for 5 min. The FLIR C3-X thermal camera was used to monitor the temperature of the sample every 30 s. The photothermal conversion efficiency of PDA–PVAMBs was determined according to the previous study.[32]

2.5 Enzymatic activity and O_2 release of PDA–PVAMBs@GOx

Various concentrations of PDA–PVAMBs@GOx of 0, 0.625×10^7, 1.25×10^7, 2.5×10^7, 5.0×10^7 and 1.0×10^8 counts/mL were mixed with 1 mg/mL glucose and incubated for 1 h, respectively. After centrifugation, H_2O_2 concentration, O_2 concentration, and pH of the subnatant were measured using H_2O_2 assay kit, portable dissolved oxygen meter and pH meter, respectively. To test the modulation of enzymatic activity by NIR irradiation, 0.5×108 counts/mL PDA–PVAMBs@GOx were mixed with 1 mg/mL glucose and irradiated under an 808 nm laser with various power densities of 0, 0.25, 0.5, 0.75, 1 W/cm^2 for 10 min, and H_2O_2 assay kit was utilized to measure the H2O2 concentration. Subsequently, O_2 release and enzymatic activity of PDA–PVAMBs@GOx by O_2-release were tested. 2 mL water with/without glucose (1 mg/mL) in the centrifuge tube was firstly put in a hypoxia incubator (1% O_2) for 1 h. Then, the probe of a portable dissolved oxygen meter was immersed under the water, which was sealed with a layer of paraffin oil. After 5 min, 1 mL of PDA–PVAMBs@GOx (10^8 counts/mL) were injected with a syringe, and the O_2 level was recorded for 10 min.

2.6 Cell Culture

CT26 murine colon carcinoma cell line was purchased from American Type Culture Collection (ATCC). The cells were cultured in RPMI 1640 medium containing 10% fetal bovine serum (FBS), streptomycin (100 μg/mL), and penicillin (100 U/mL) at 37 °C under humidified 5% CO_2 atmosphere. The cells were subcultured every 3 days.

2.7 *In vitro* US and enhanced PA imaging

The PDA–PVAMBs were firstly immobilized in an agarose phantom with a 3D-printed pattern for both US and PA scanning. Briefly, 50 mL of 2 % (wt/vol) agarose in distilled water was heated under 80 ℃. After the agarose was completely dissolved, the aqueous solution was transferred to the 3D-printed pattern. Different concentrations of aqueous PDA–PVAMBs (2.5×10^6 to 2×10^7 counts/mL) were mixed with the dissolved agarose solution at a ratio of 1:1. Then the pattern was removed and the mixed PDA–PVAMBs solution was poured into the empty cavities and allowed to solidify. US and PA imaging was carried out using a VEVO LAZR instrument (FUJIFILM VisualSonics, Amsterdam, NL), operating with an LZ250 transducer at the frequency of 21 MHz for US imaging and 700 nm wavelength for PA imaging. To evaluate the enhanced PA performance and PA stability of PDA–PVA MBs, water, PVAMBs, PDA NPs, PDA NPs + PVAMBs, PDA–PVAMBs, and PDA–PVAMBs (collapsed) solutions in PE tubes were imaged at a PA laser fluence of 25 mJ/cm^2. To ensure the comparison was performed with the same PDA concentration, PDA NPs and PDA–PVAMBs should have the same optical density (O.D.) at 700 nm, where O.D. of PDA–PVAMBs was determined after collapsing by sonication to eliminate the optical scattering effect by MBs. Afterward, PDA NPs and PDA–

PVAMBs with the same O.D. (0.5, 1.0, 1.5, 2.0) at 700 nm were measured to calculate the PA magnification. Here, PDA NPs with an average size of 70 nm were synthesized according to the previous study.[36]

2.8 Hemocompatibility test

Red blood cells (RBCs) were isolated from the whole blood of mice by centrifuging a mixture of whole blood and ringer's solution at 500 g for 10 min. The washing step was repeated 3 times and the RBCs were resuspended in PBS buffer. RBCs with a final concentration of 10^6 cells/mL were incubated with different concentrations of PDA–PVAMBs@GOx (0.2×10^7, 0.4×10^7, 0.6×10^7, 0.8×10^7, 1.0×10^7 counts/mL) at 37 ℃ for 3 h, while RBCs incubated with PBS and distilled water were regarded as positive and negative controls, respectively. Then, the mixture was centrifuged to let the MBs float and uncracked RBCs precipitate. The absorbance of each sample at 570 nm with a reference at 655 nm was measured using a microplate reader to calculate the hemolysis degree in each group.

2.9 *In vitro* cytotoxicity study

CT26 cells were first seeded in a 96-well plate at a density of 5000 cells per well for 24 h to evaluate the *in vitro* toxicity of PDA–PVAMBs and PDA–PVAMBs@GOx with TPZ and NIR irradiation. The culture medium was then removed and fresh medium (control) and fresh medium containing different concentrations (from 2×10^6 to 1.0×10^7 counts/mL) of PDA–PVAMBs, PDA–PVAMBs@GOx, and PDA–PVAMBs@GOx–TPZ (TPZ: 2 μg/mL) were added. Free TPZ varies from 0.2 to 2 μg/mL was also introduced cell treatment. After 4 h of incubation, the 808 nm laser with a power density of 1 W/cm^2 was used to irradiate the PDA–PVAMBs@GOx and PDA–PVAMBs@GOx–TPZ groups for 10 min, and then continued to incubate for another 24 h. Finally, a cell counting kit-8 (CCK-8) kit assay was used to determine the cell viability.

2.10 Live/dead cell staining assay

CT26 cells were seeded into a 96-well plate until the cell density reached 2×10^5 cells/well. The cells were then treated with PDA–PVAMBs, PDA–PVAMBs@GOx, and PDA–PVAMBs@GOx–TPZ, in which all groups had the same concentration of 107 counts/mL. All samples were then incubated for 6 h. The illumination group was under an 808 nm laser (0.5 W/cm^2) for 10 min. Then, these different groups of cells were incubated for another 4 h, and stained with Live/dead™ Cell Imaging Kit (Invitrogen™) for 15 min. A Nikon Eclipse Ti2-E Live-cell Fluorescence Imaging System was used for further analysis.

2.11 Intracellular ROS and hypoxia staining assay

CT26 cells were seeded into a 96-well plate until the cell density reached 2×10^5 cells/well. Image-iT™ Hypoxia Reagent (Invitrogen™) was first added to the cells and incubated for 30 min, then the culture medium containing Image-iT™ Hypoxia Reagent was replaced with fresh medium and subsequently incubated in hypoxia incubator (1% O_2), fresh medium containing H_2O_2 (200 μM), and PDA–PVAMBs@GOx (10^7 counts/mL) and incubated for an additional 4 h, respectively. CellROX™ Deep Red Reagent and Hoechst were then utilized to stain ROS and cell nuclei for 15 min for further observation by a Nikon Eclipse Ti2-E Live-cell Fluorescence Imaging System. As a supplementary, ROS generation of CT26 cells after treated with PDA-PVAMBs + PTT and PDA-PVAMBs@GOx + PTT were also studied to confirm the enhanced enzymatic activity.

2.12 Animal tumor xenograft model

BALB/c mice (4-6 weeks old, female) were bought from Centralized Animal Facilities of The Hong Kong Polytechnic University. All animal protocols were conducted under the Guidelines for Care and Use of Laboratory Animals of "The Special Health Service, Department of Health, Hong Kong Special Administrative Region" and approved by the Animal Ethics Committee of "The Hong Kong Polytechnic University" (19-20/61-BME-R-GRF). CT26 cells (0.1 mL, 2×10^7 cells/mL in serum-free medium) were injected subcutaneously to the back of mice.

2.13 *In vivo* US and PA imaging

US and PA imaging were used to monitor the injected PDA–PVAMBs@GOx and the vascular saturated O_2 (sO_2) in the tumor site for 7 days. When the tumor volume reached 100 mm^3, mice were intratumorally injected with PDA–PVAMBs@GOx and US/PA imaging was performed with a VEVO LAZR Imaging System at 0 h, 12 h, 1 day, 2 days, 4 days, and 7 days of post-injection.

2.14 *In vivo* photothermal imaging and antitumor study

When the size of the tumor reached 100 mm^3, the tumor-bearing mice were divided into 5 groups (each group contained 5 nude mice) and were processed as follows: (1) PBS; (2) PDA–PVAMBs@GOx; (3) PDA–PVAMBs@GOx–TPZ; (4) PDA–PVAMBs@GOx + Laser; (5) PDA–PVAMBs@GOx–TPZ + Laser. For group (1), 100 μL PBS was directly injected into the CT26 tumor, and for group (2) to group (5), 100 μL PDA–PVAMBs@GOx (10^8 counts/mL) were injected intratumorally. 12 h after, CT26 tumor-bearing nude mice in group (3) and (5) were injected with 100 μg TPZ while in group (4) and (5), tumors were irradiated with an 808 nm NIR laser with a power density of 0.5 W/cm^2 for 10 min. During the 10-min laser irradiation, IR thermal imaging camera was utilized to monitor the temperature changes of the tumors in different groups. The whole therapy procedure was repeated on day 4. Tumor sizes and body weights of the tumor-bearing mice were recorded every 2 days, and the tumor size was calculated according to the formula: volume = width^2 × length / 2. After 14 days, the mice in each group were euthanized, and the tumors and major organs (heart, liver, spleen, lung, and kidney) were taken out. Tumors were weighed, fixed, embedded, and sectioned for further hematoxylin and eosin (H&E) staining and TUNEL immunofluorescence staining. Other organs were sectioned for H&E staining. To confirm the in-situ activation of hypoxia, tumor sections were obtained for HIF-1α immunofluorescence staining 12 h after the injection of PDA–PVAMBs@GOx.

2.15 Statistical analysis

Data were expressed as mean ± standard deviation (SD). Student's t-test and One-way analysis of variance (ANOVA) were utilized to analyze the significance between groups, where significant differences were defined as *P < 0.05, **P < 0.01, and ***P < 0.001.

3. Results and Discussion

3.1 Preparation and characterization of PDA–PVAMBs@GOx

The one-pot synthesis scheme of PDA–PVAMBs@GOx is shown in Fig. 1a. Firstly, PVA long chains undergo oxidative cleavage by $NaIO_4$ and are split into telechelic PVA chains. Dopamine hydrochloride is then mixed with the solution with telechelic PVA chains and homogenized at high speed. During the vigorous homogenizing, bubbles are largely generated in the solution and immediately wrapped and stabilized by amphiphilic telechelic PVA chains. Then, the telechelic PVA chains are acetalized and crosslinked around air bubbles to form an interfacial layer. Meanwhile, dopamine hydrochloride is oxidized by the residual NaIO4 and polymerized along with PVA cross-linking to form PDA–PVAMBs. Finally, GOx is firmly attached to polydopamine on MBs by covalent bonds between amino groups on GOx and catechol on PDA through Schiff base reaction to form PDA–PVAMBs@GOx.[37]

The as-synthesized PDA–PVAMBs showed black color in solution, which was different from the white color of pure PVAMBs (Fig. S1a). Similar to PVAMBs, PDA–PVAMBs were very stable and easy to store compared with lipid MBs. Moreover, PDA–PVAMBs do not need to be filled with perfluorocarbon gas such as lipid or protein-based MBs to maintain stability,[38,39] and could be synthesized on a large scale and stored at room temperature for more than 1 month without obvious breakage or morphology change (Fig. S1b). After synthesis, the concentrated PDA–PVAMBs were lyophilized and weighed. The estimated mass of every 10^8 PDA–PVAMBs was about 1 mg. The SEM image shows a uniform size distribution of PDA–PVAMBs with smooth surfaces (Fig. 1b). Confocal laser scanning microscopy (CLSM) image of PDA–PVA MBs shows a clear and complete hollow structure with good water dispersion (Fig. 1c and 1d). UV–Vis–NIR spectroscopy shows that PDA–PVAMBs have higher extinction amplitudes in the full spectrum compared with that of PDA NPs due to the scattering of MBs (Fig. 1e). Dynamic light scattering (DLS) measurement reveals that the average size of PDA–PVAMBs is about 3.5 μm (Fig. S2a). Compared with pure PVAMBs, the size of PDA–PVAMBs shows a slight increase due to PDA doping, while loading of GOx shows no obvious further increase in size. The diameters of the PDA-PVAMBs@GOx in culture medium containing FBS were slightly larger than those of PDA-PVAMBs@GOx in distilled water or PBS, which could attribute to protein binding on the surface of the PDA-PVAMBs@GOx (Fig. S2b). For zeta potential measurement, the surface charge of PDA–PVAMBs is more negative compared to that of PVAMBs due to additional phenol compounds on the surface (Fig. 1f). After the conjugation of GOx, the zeta potential was shifted from -32.4 mV to -18.4 mV. The FTIR spectra measurements were also performed to demonstrate the doping of polydopamine. As shown in Fig. 1g, the broad absorption band at 3 000–3 600 cm^{-1} represented various types of hydrogen bonding interactions of PVAMBs.

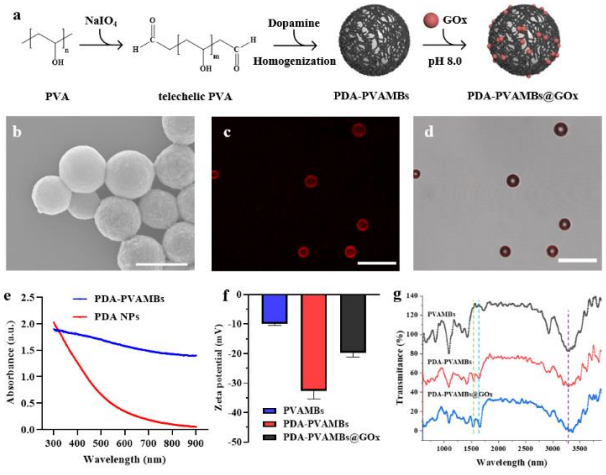

Fig. 1 Fabrication and characterization of PDA-PVAMBs@GOx. (a) Synthesis scheme of PDA–PVAMBs@GOx (b) FESEM image of PDA–PVAMBs. Scale bar: 3 μm. (c) and (d) Representative CLSM images of PDA–PVA MBs, the shell was stained by RBITC. Scale bars: 20 μm. (e) UV–Vis–NIR Spectra of PDA–PVAMBs and PDA NPs. (f) Zeta potential of PVAMBs, PDA-PVAMBs and PDA-PVAMBs@GOx. (g) FTIR spectra of PVAMBs, PDA-PVAMBs and PDA-PVAMBs@GOx.

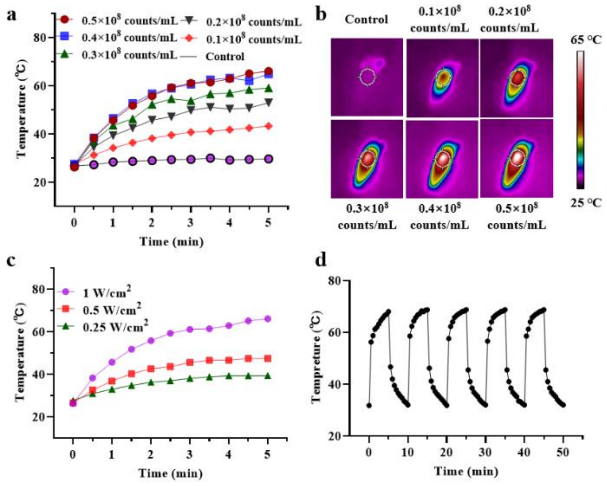

Fig. 2 Phothothermal effect of PDA-PVAMBs. (a) Temperature change with time at various concentrations (0.1-0.5×10^8 counts/mL) of PDA–PVAMBs under 808 nm laser irradiation (1 W/cm^2). (b) IR thermographic images of PDA–PVAMBs (0.1-0.5×10^8 counts/mL) under 808 nm laser irradiation (1 W/cm^2) after 5 minutes. (c) Temperature change of 0.5×10^8 counts/mL PDA–PVAMBs under 808 nm laser irradiation with various power densities (0.25, 0.5, 1 W/cm^2). (d) Photothermal stability of PDA–PVAMBs (0.5×10^8 counts/mL) under 808 nm laser irradiation with a power density at 1 W/cm^2 for 5 cycles.

After PDA doping, peaks at 1,506 and 1,616 cm^{-1} appeared for the formation of amide N–H shearing vibration and benzene skeleton vibration, respectively. GOx modification hardly changed the absorption spectra due to the relatively low weight ratio and no formation of new bonds. Afterwards, the loading capacity of GOx was around 15.3 μg per 10^8 PDA–PVAMBs@GOx determined by the BCA Protein Assay Kit. Hence, zeta potential measurement, FTIR spectra, and BCA protein assay demonstrated the successful formation of PDA–PVAMBs@GOx.

3.2 *In vitro* photothermal characteristics of PDA–PVAMBs

To evaluate the photothermal capability of PDA–PVAMBs, different concentrations of PDA–PVAMBs (0.1, 0.2, 0.3, 0.4, and 0.5×10^8 counts/mL) were irradiated by an 808 nm NIR laser at 1 W/cm^2 for 5 min. PDA–PVAMBs showed a concentration-dependent photothermal property (Fig. 2a, 2b). At the concentration of 0.5×10^8 counts/mL, the temperature of the PDA–PVAMBs solution was raised from room temperature to a steady plateau around 65 ℃ after 5 min of laser irradiation (Fig. 2a). Correspondingly, the temperature in the distilled water group showed no significant change (< 5 ℃). Moreover, PDA–PVAMBs also showed a power-density dependent feature (Fig. 2c). When the concentration of PDA–PVAMBs was fixed at 0.5×10^8 counts/mL, NIR irradiation with a power density of 1 W/cm^2, 0.5 W/cm^2, and 0.25 W/cm^2 for 5 min showed a final temperature at 65 ℃, 47 ℃, and 40 ℃, respectively. Besides, when the PDA–PVAMBs sample was irradiated in cycles, the temperature rise-decrease curve of the sample remains stable, indicating the high photothermal stability for continuous laser illumination (Fig. 2d). Furthermore, the photothermal conversion efficiency of PDA–PVAMBs was calculated as 41.3% (Fig. S3). The modification of GOx showed no obvious influence on the photothermal conversion of PDA–PVAMBs (Fig. S4).

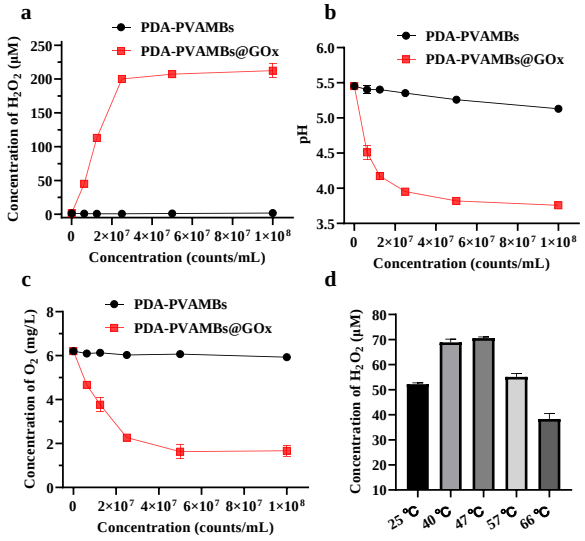

Fig. 3 Enzymatic activity assay of PDA-PVAMBs and PDA-PVAMBs@GOx. Concentration of H_2O_2 (a), pH change (b), and concentration of dissolved O_2 (c) generating from 1 h reaction between various concentrations (0.625×10^7-10^8 counts/mL) of PDA–PVAMBs/PDA–PVAMBs@GOx and 1 mg/mL glucose at room temperature. (d) GOx enzymatic activity of PDA–PVAMB@GOx (0.5×10^8 counts/mL) mixing with glucose (1 mg/mL) represented by the yield of H_2O_2 under different temperatures by NIR laser irradiation for 10 min.

3.3 *In vitro* enzymatic activity assay of PDA–PVAMBs@GOx

GOx acts as a trigger point for starvation and hypoxia-activated therapy. Therefore, the enzymatic activity of PDA–PVAMBs@GOx is important for the success of combinational therapy in this study. The generated H_2O_2, decreased pH value, and depleted O_2 are used as indicators to evaluate the enzymatic activity of PDA–PVAMBs@GOx. Generally, the enzymatic activity of PDA–PVAMBs@GOx showed a concentration-dependent feature (Fig. 3). With the increase of PDA–PVAMBs@GOx concentration, H_2O_2 concentration in the solution increased sharply at first and then reached a plateau with a slow increase after 0.25×10^8 counts/mL (Fig. 3a). As shown in Fig. 3b, the pH value of the solution decreased below 4.0 when the concentration of PDA–PVAMBs@GOx increased to 0.25×10^8 counts/mL. The optimum pH value for the enzymatic activity of GOx was generally around 5.5 and the efficient enzymatic activity range of GOx was from pH 4.0 to 7.0.[13] The low pH value below 4.0 led to low enzymatic activity of GOx, which explained the slow increase of H_2O_2 concentration with further increase of PDA–PVAMBs@GOx concentration above 0.25×10^8 counts/mL in Fig. 3a. The decrease of O_2 concentration in the solution was also observed due to the consumption of O_2 during glucose decomposition (Fig. 3c). In contrast, unmodified PDA–PVAMBs had no obvious effects on H_2O_2 concentration, pH value, and O_2 level.

Since PTT is involved in the entire theranostics process, the thermal stability and enzymatic activity of PDA–PVAMBs@GOx under NIR irradiation should be evaluated. In this experiment, H_2O_2 concentration in the solution with PDA–PVAMBs@GOx (0.5×10^8 counts/mL) was measured upon NIR irradiation with various power densities of 0, 0.25 W/cm^2, 0.5 W/cm^2, 0.75 W/cm^2 and 1 W/cm^2 for 10 min, which corresponded to temperatures of 25 ℃, 40 ℃, 47 ℃, 57 ℃ and 66 ℃, respectively. It was observed that enzymatic activity of PDA–PVAMBs@GOx first increased with the increase of temperature, reached the maximum between 40 ℃ and 47 ℃, and then decreased with the further increase of temperature (Fig. 3d). The results of temperature effects on enzymatic activity of GOx matched the previous studies that the conjugation of GOx on micro/nanomaterials would stabilize the enzyme structure and activity against high temperature. Furthermore, as the temperature increased, the enzymatic reaction was even accelerated.[20, 24] Hence, the low-temperature PTT could not only maintain the activity of GOx, but also increase the catalytic effect of GOx.

To evaluate the O_2-carrying capacity and O_2-release promoted enzymatic activity of PDA–PVAMBs@GOx, the O_2

concentration change of oxygen-depleted water with the addition of PDA–PVAMBs@GOx with/without glucose was measured (Fig. S5). It was observed that the O_2 concentrations of both oxygen-depleted water with or without glucose were initially at a very low value. For the group of O_2-depleted water without glucose, the O_2 concentration in the O_2-depleted water quickly increased (~65%) at the first 2 min after adding PDA–PVAMBs@GOx, then gradually increased to a plateau within 5 min. For the group of O_2-depleted water with glucose, the addition of PDA–PVAMBs@GOx also quickly increased at the first 2 min but then started to decline due to the O_2 consumption during glucose decomposition by GOx. The results demonstrated the O_2-carrying capacity of PDA–PVAMBs@GOx, which could effectively promote GOx-based enzymatic reaction.

3.4 *In vitro* US and enhanced PA imaging

PA imaging signals of PDA–PVAMBs were first tested in an agarose-based phantom test in situ, which could mimic biological tissues with minimized background noise.[40] Different concentrations of PDA–PVAMBs (0, 0.125×10^7, 0.25×10^7, 0.5×10^7 and 1×10^7 counts/mL) were mixed in agarose gel solution, respectively. The mixed solution was then injected in the groove of an agarose gel block to generate tissue-like phantoms (Fig. S6). The agarose gel block was shaped by a 3D-printed mold. With the increase of concentrations of PDA–PVAMBs, both B-mode US and PA imaging signals were enhanced proportionally (Fig. 4a, 4b). Here, US imaging contrast capability is attributed to PVAMBs, and PA imaging contrast capability is attributed to doped PDA in the interfacial layer.

We then evaluated if PDA doping on PVAMBs could enhance PA signals compared with dispersed PDA NPs. PA imaging signals of 6 groups including water, PVAMBs, PDA NPs, PVAMBs mixed with PDA NPs (PVAMBs + PDA NPs), PDA–PVAMBs, and collapsed PDA–PVAMBs after sonication are shown in Fig. 4c and 4d. Here, the group of PDA–PVAMBs contained the same amount of PDA as the group of PDA NPs. It was observed that the groups of water and PVAMBs showed no obvious PA amplitudes. PDA NPs exhibited moderate PA amplitudes due to their photothermal conversion capability. The mixing of PDA NPs with PVAMBs (PVAMBs + PDA NPs) had no additional PA amplitudes since PVAMBs did not provide PA contrast. However, when PDA was doped inside the surface layer of PVAMBs (PDA–PVAMBs), the PA amplitudes largely increased. It could be explained by the following factors. Firstly, PDA was doped in the shell of MBs, resulting in the local agglomeration of PDA with thermal field overlap and fast heat transfer to enhance PA amplitudes.[41-42] Secondly, the heat generated in the liquid-gas interface might generate nanobubbles due to the local high temperature and promote the PA amplitude.[33] Finally, the generated acoustic waves from PDA triggered the oscillation of MBs near the resonance frequency, generating additional acoustic waves for PA enhancement.[33,34] To further demonstrate the enhancement effect by the MBs. PDA–PVAMBs were collapsed by sonication. PA amplitudes of collapsed PDA–PVAMBs decreased to 40% of that of the PDA–PVAMBs due to the disappearance of the MBs oscillation enhancement effect and the still existed local agglomeration effect (Fig. 4d). With the same PDA content (the same O.D. at 700 nm), PDA–PVAMBs showed PA signal amplification by 6.5-

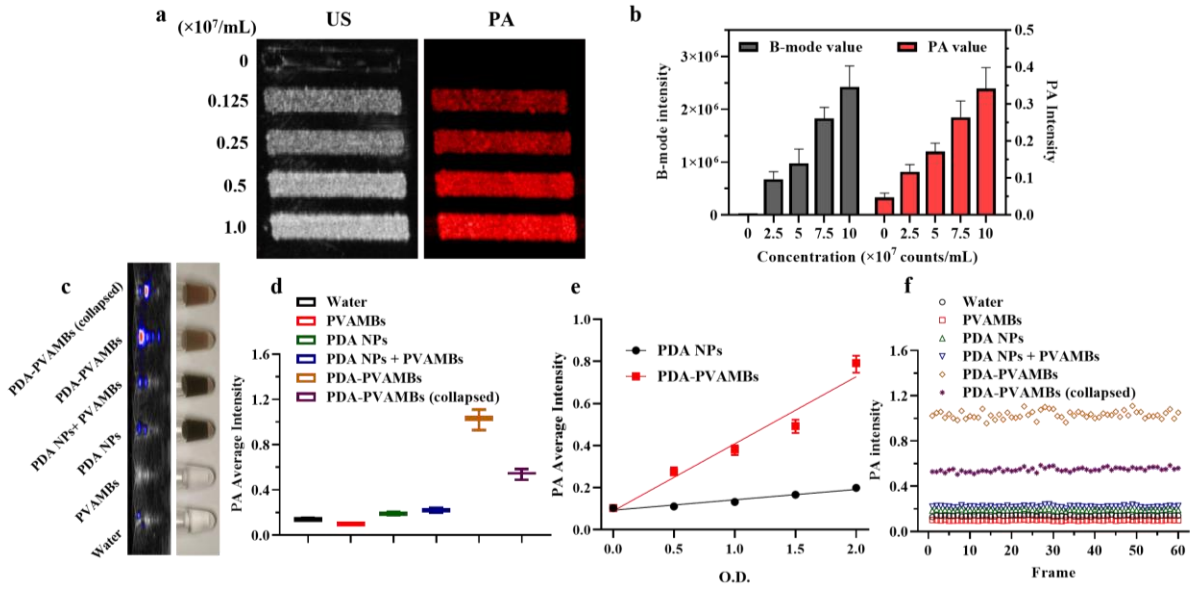

Fig. 4 (a) US and PA imaging of various concentration of PDA–PVAMBs (0, 0.125, 0.25, 0.5 and 1×10^7 counts/mL) in agarose phantom. (b) Quantified US and PA amplitudes of various concentrations of PDA–PVAMBs in agarose phantom. (c) PA and optical imaging of aqueous dispersions with water, PVAMBs, PDA NPs, PDA NPs + PVAMBs, PDA–PVAMBs, and PDA–PVAMBs (collapsed) in PE tubes, respectively. PDA NPs and PVAMBs had an equal O.D. at 700 nm. (d) Quantified PA average amplitudes and (e) PA average amplitudes of PDA NPs and PDA–PVAMBs with same O.D. at 700 nm (n = 10). All O.D. of PDA–PVAMBs was determined after collapsing by sonication. (f) PA stability of water, PVAMBs, PDA NPs, PDA NPs + PVAMBs, PDA–PVAMBs, and PDA–PVAMBs (collapsed), respectively (n = 60).

fold compared with PDA NPs (Fig. 4e). Previous studies reported an enhanced PA performance using plasmonic nanoparticle-templated lipid MBs.[33] In that study, PA signals exhibited a 5.4-fold increased amplitude but suffered from the instability of lipid MBs under laser irradiation. The instability greatly restricted plasmonic NPs templated lipid MBs for long-term and stable US/PA monitoring. In contrast, our PDA–PVAMBs showed good stability for PA amplitudes during continuous laser irradiation, which were suitable for long-term monitoring (Fig. 4f).

3.5 The hemocompatibility and cytotoxicity of PDA–PVAMBs

Biocompatibility of PDA–PVAMBs was demonstrated from haemocompatibility and cytotoxicity. For haemocompatibility testing, PDA–PVAMBs@GOx with different concentrations (0 to 1×10^7 counts/mL) were mixed and cultured with RBCs. No obvious hemolysis was observed even at the highest concentration compared with the PBS-treated positive control group (Fig. 5a and Fig. S7). For cytotoxicity testing, PDA–PVAMBs with various concentrations were cultured with CT26 colon carcinoma cells *in vitro* for 24 h and high cell viability over 95% was observed for PDA–PVAMBs even with the highest concentration of 1×10^7 counts/mL (Fig. 5b). Therefore, PDA–PVAMBs were demonstrated to have good biocompatibility.

3.6 *In vitro* synergistic therapy

The *in vitro* synergistic therapeutic effect of PDA–PVAMBs@GOx–TPZ under NIR irradiation with various concentrations was then evaluated on CT26 cells through CCK-8 kit assay. Three other groups of PDA–PVAMBs@GOx–TPZ without NIR irradiation, PDA–PVAMBs@GOx with NIR irradiation and PDA–PVAMBs@GOx without NIR irradiation were set for comparison (Fig. 5c). The NIR laser treatment was conducted with a low power density at 0.5 W/cm^2 for 10 min to ensure a low temperature for PTT. It was found that the therapeutic effect was dependent on different treatment patterns. The therapeutic effect of PDA–PVAMBs@GOx (w/o TPZ + w/o NIR) was only based on starvation and the cell viability moderately decreased to 69% at a concentration of 1×10^7 counts/mL (Fig. 5c). The catalytic decomposition of glucose in PDA–PVAMBs@GOx treated cells was then evaluated with a ROS-sensitive fluorescent probe (CellROX™ Deep Red Reagent, dark red fluorescence) and a hypoxia-sensitive fluorescent probe (Image-iT™ Green Hypoxia Reagent, green fluorescence) (Fig. 5d). CT26 cells cultured in a control (normoxia) environment showed no obvious red or green fluorescence. CT26 cells cultured in hypoxia environment (1% O_2) or normoxia environment with 200 μM H_2O_2 only had green fluorescence or red fluorescence, attributed to the intracellular hypoxia and ROS, respectively. In contrast, cells treated with PDA–PVAMBs@GOx exhibited both red and green fluorescence, indicating that GOx on the surface of MBs catalyzed the decomposition of glucose with O_2 to produce H_2O_2 and local hypoxia. The generated intracellular hypoxia could further trigger the cytotoxicity of TPZ drug. Hence, the cell viability of CT26 cells treated with PDA–PVAMBs@GOx–TPZ further decreased to 48% (Fig. 5c). In contrast, no obvious cytotoxicity was found for cells even treated with a high concentration of TPZ (2 μg/mL), indicating that PDA–PVAMBs@GOx could trigger the toxicity of TPZ (Fig. S8). Besides, the combination of PDA–PVAMBs@GOx with PTT therapy (under 808 nm laser irradiation at 0.5 W/cm^2 for 10 min) also decreased the cell viability to 51% (Fig. 5c). To demonstrate the promotion of enzymatic activity of PDA–PVAMB@GOx by photothermal treatment, intracellular ROS was measured for CT26 cells treated with PDA-PVAMBs@GOx (only GOx effect), PDA-PVAMBs+laser (only PTT effect) and PDA-PVAMBs@GOx+laser (GOx+PTT) (Fig. S9). The group

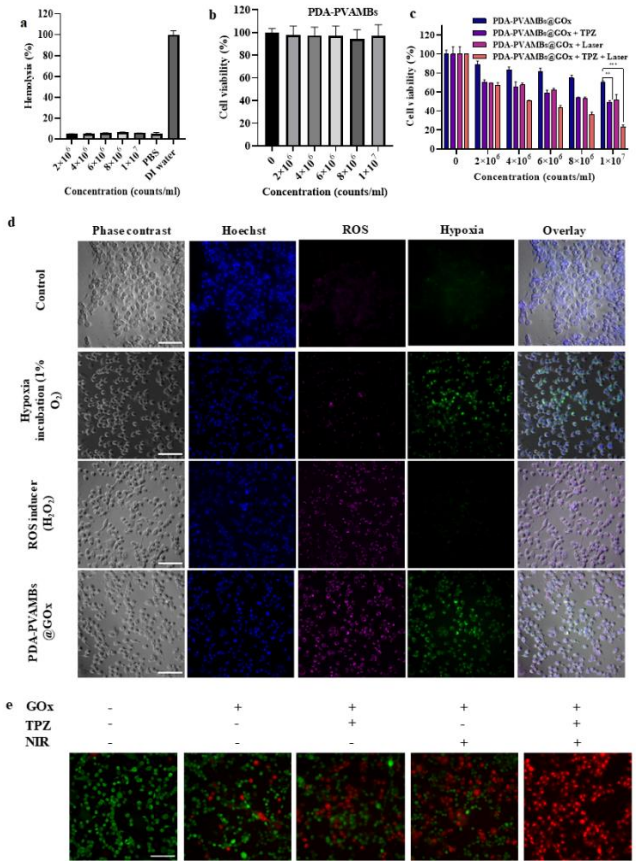

Fig. 5 *In vitro* cytotoxicity and intracellular ROS/Hypoxia generation. (a) Haemocompatibility of various concentrations of PDA–PVAMBs@GOx (b) Cytotoxicity of various concentrations of PDA–PVAMBs. (c) Cell viability of various concentrations of PDA–PVAMBs@GOx, PDA–PVAMBs@GOx–TPZ, PDA–PVAMBs@GOx + Laser, and PDA–PVAMBs@GOx–TPZ + Laser. The NIR laser power density was 0.5 W/cm^2 for 10 min. $^{**}P < 0.01$, and $^{***}P < 0.001$ (d) Representative fluorescent images of CT26 cells stained by Hoechst, CellROX™ reagent, and Image-iT™ Hypoxia reagent incubated 4 h in normoxia, hypoxia (1% O_2), 200 μM H_2O_2 and 1.0×10^7 counts/mL of PDA–PVAMBs@GOx, respectively. Scar bars: 50 μm. (e) Representative live/dead cell images of CT26 cells treated with PBS, PDA–PVAMBs@GOx–TPZ, PDA–PVAMBs@GOx + Laser, and PDA–PVAMBs@GOx–TPZ + Laser. Scar bars: 50 μm.

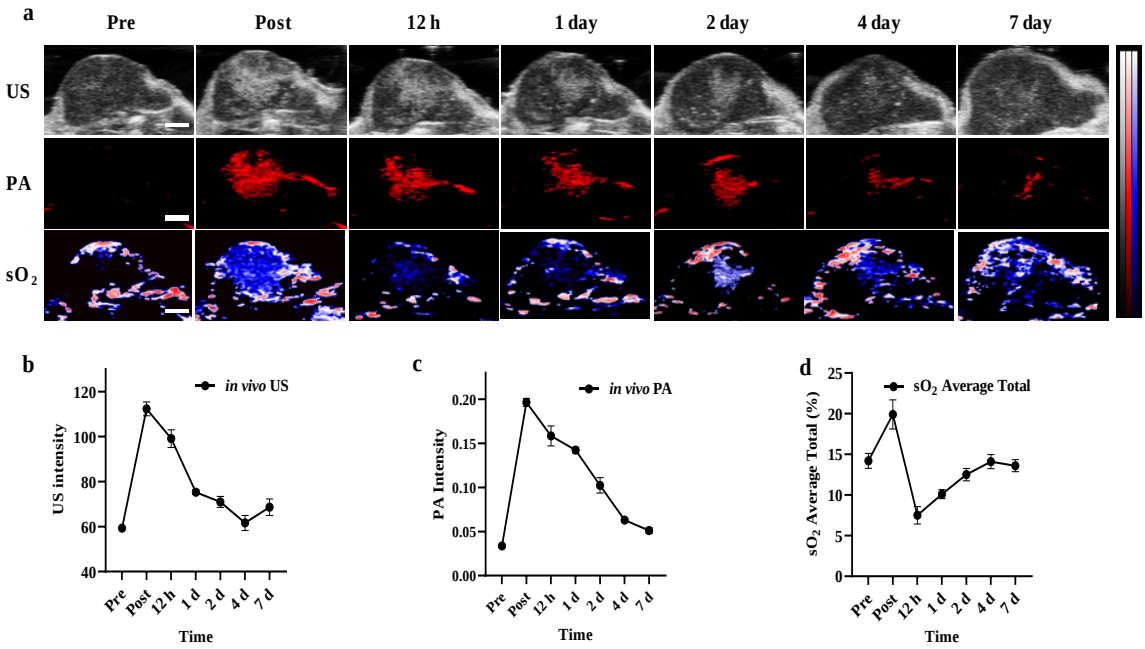

Fig. 6 *In vivo* US/PA/sO2 imaging. (a) *In vivo* multimodality US/enhanced PA imaging of tumor after intratumoral injection of PDA–PVAMBs@GOx including B-mode US imaging, PA imaging of PDA–PVAMBs@GOx, and PA imaging of sO_2 average total. Quantitative analysis of the B-mode US imaging signal (b), PA imaging of PDA–PVAMBs@GOx (c), and PA imaging of sO_2 average total (d) after intratumoral injection of PDA–PVAMBs@GOx from day 0 to day 7 (n = 5). Scale bars: 1 mm.

treated with PDA-PVAMBs@GOx generated intracellular ROS due to the enzymatic reaction by the loaded GOx. The group treated with PDA-PVAMBs+laser generated very weak ROS signal due to no GOx reaction. In contrast, the group treated with PDA-PVAMBs@GOx+laser generated even stronger fluorescent signals compared to that of the group treated with PDA-PVAMBs@GOx, indicating that PTT could reinforce the enzymatic activity of PDA-PVAMBs@GOx with a synergistic effect. The above results demonstrated that the combination of two therapeutic methods (starvation + TPZ or starvation + PTT) achieved synergistic and enhanced therapeutic effects. Finally, when three therapeutic methods were combined (starvation + TPZ + PTT), the cell viability sharply dropped off to 21% with the best therapeutic effect (Fig. 5c). To further confirm, fluorescence live/dead cell assay was employed to observe the combinational therapy effects. As shown in Fig. 5e, when PDA–PVAMBs were incubated with cells, only green fluorescence was observed. In contrast, PDA–PVAMBs@GOx group (w/o TPZ + w/o NIR) showed obvious red fluorescence, indicating the starvation therapy effect. The dual combinational therapy of starvation + PTT and starvation + TPZ further enhanced the therapeutic effect with the higher ratio of red fluorescence. Finally, almost all the CT26 cells treated with starvation + PTT + TPZ exhibited strong red fluorescence, indicating the superior therapeutic efficacy of the triple combinational therapy.

This high therapy efficacy is attributed to the synergistic effect of the three combined therapeutic approaches. GOx on the surface of MBs first decomposes the nutrient source glucose in the culture medium, consumes O_2, and produces cytotoxic H_2O_2. Simultaneously, the external NIR irradiation raises the overall environmental temperature moderately, which eliminates cancer cells through photothermal effect and elevates the activity of GOx. As the O_2 in the culture medium is consumed to generate local hypoxia, the cytotoxicity of TPZ is activated to further kill the cancer cells. The three therapies complement each other and reduce the concentration of PDA–PVAMBs@GOx–TPZ and laser intensity, which may help to further reduce the in vivo systemic toxicity.

3.7 *In vivo* US and enhanced PA imaging

Dual-modality US/PA imaging was used for real-time in vivo monitoring of PDA–PVAMBs@GOx inside the tumor (Fig. 6). US/PA signals of PDA–PVAMBs@GOx and sO_2 PA signals were imaged at various time points (Fig. 6a). US signals were well maintained at the original 12 h post-injection and then started to decrease gradually until almost disappeared after 7 days (Fig. 6a, 6b). PA signal of PDA–PVAMBs@GOx showed a slow decrease at the original 24 h post-injection and then gradually decreased until almost disappeared after 7 days (Fig. 6a, 6c). The decrease of US contrast signal after 12 h of injection was due to the breaking and degradation of PDA–PVA MBs@GOx into small pieces in the physiological environment. PDA doped small membrane pieces after MB breaking could still generate PA imaging signals in the tumor site, explaining the maintained

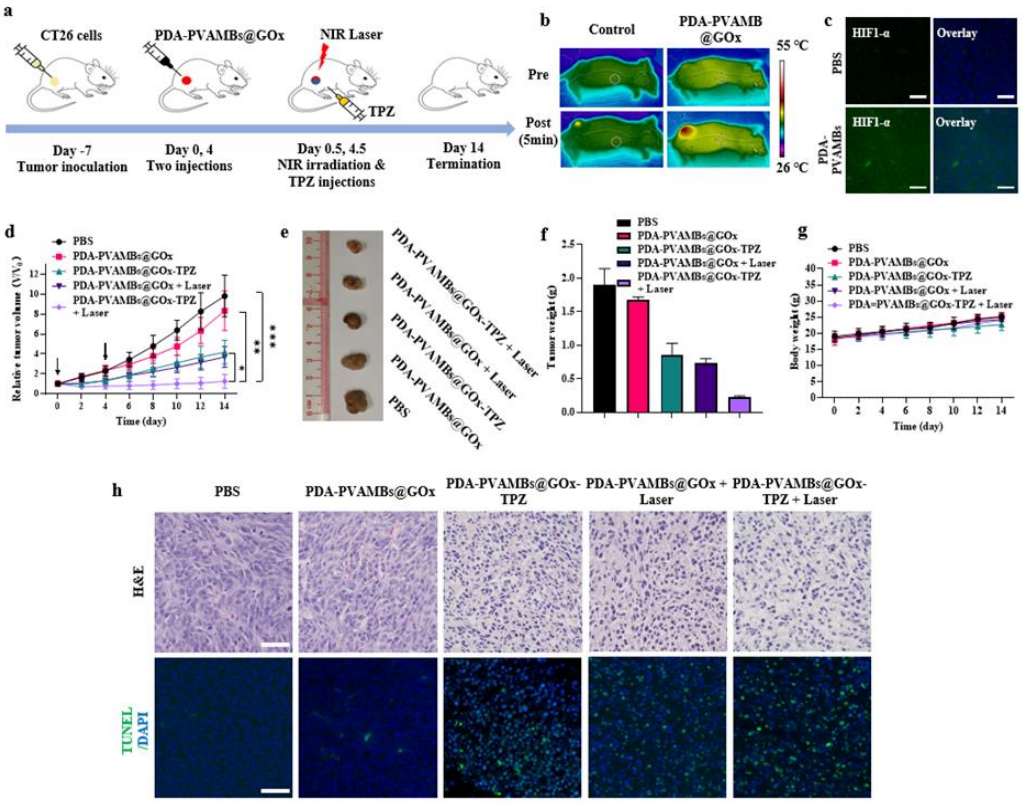

Fig. 7. *In vivo* antitumor effect. (a) Schematic illustration of experimental design for *in vivo* therapy in mice bearing CT26 tumor. (b) IR thermographic images of tumor-bearing mice before & after intratumoral injection of various samples under NIR irradiation (808 nm, 0.5 W/cm^2) for 10 min. (c) HIF1-α immunostaining of tumor slice after treatment with PBS and PDA–PVAMBs@GOx, respectively. Scale bars: 50 μm. (d) The relative tumor volume changes over 14 days under various treatments (n = 5). *P < 0.05, **P < 0.01, and ***P < 0.001 (e) Representative photographs of the excised solid tumors from various groups on day 14. (f) The tumor weight at day 14 under various treatments (n = 5). (g) The body weight change of tumor-bearing mice over 14 days under various treatments (n = 5). (h) Histological analysis of the slices from solid tumors on day 14 via H&E staining and TUNEL assays. Scale bars: 50 μm.

high PA signals at day 1. When PDA doped small membrane pieces were further degraded and cleared out from the tumor site after day 1, PA imaging signals were further decreased. For the tumor O_2 level, sO_2 signals enhanced from 14.8% to 19.7% after the injection of PDA–PVAMBs@GOx due to the release of O_2, and then reached the lowest point (7.5%) at 12 h post-injection due to the glucose depletion process by GOx (Fig. 6a, 6d). Therefore, hypoxia-prodrug TPZ could be chosen to be intratumorally injected at 12 h post-injection of PDA–PVAMBs@GOx to ensure the high therapy efficacy. Afterward, the sO_2 level in the tumor gradually increased until came back to 13.6% after 7 days by the slow clearance of PDA–PVAMBs@GOx and the continuous diffusion of oxygen from outside. The above in vivo US/PA imaging results demonstrated the long-term retention of PDA–PVAMBs@GOx in vivo and indicated the best TPZ injection and NIR treatment time was around 12 h post-injection of PDA–PVAMBs@GOx.

In practice, US/PA imaging can help for precise treatment by providing guidance on the treatment procedure. Briefly, US/PA imaging could be used to verify proper injection of therapeutic agents and determine the specific location of PDA–PVAMBs@GOx. For laser-based PTT treatment step, laser irradiation could be induced to cover the whole tumor area to prevent the misalignment of the laser irradiation site and the therapytic agent injection site. For the following TPZ injection step, US/PA imaging could monitor the change of tumor sO2 level and determine the appropriate time for TPZ injection. Therefore, multiple treatment procedures can be completed under the guidance of dual-mode US/PA imaging, which may ensure the therapy efficacy.

3.8 *In vivo* synergistic therapy

The in vivo therapeutic effect was investigated by intratumoral injection of PDA–PVAMBs@GOx. Five groups of CT26 tumor-bearing mice were used in this study. In the treatment groups, mice were intratumorally injected with PDA–PVAMBs@GOx (10^8 counts/mL, 100 μL), with or without low-power NIR irradiation (808 nm at 0.5 W/cm^2 for 10 min) and TPZ (100 μg)

was intratumorally injected 12h after PDA–PVAMBs@GOx administration. The same treatments were repeated on day 4 (Fig. 7a). IR thermographic images were taken to monitor temperature changes of tumors during laser irradiation (Fig. 7b). For the mice treated with PDA–PVAMBs@GOx, tumor temperature increased to about 48 ℃ rapidly after 10-min irradiation. In contrast, the tumor temperature of the control group injected with PBS did not change obviously. Moreover, HIF-1α immunofluorescence staining showed strong green fluorescence in the group treated with PDA–PVAMBs@GOx compared with the control group, indicating the generation of in-situ hypoxia (Fig. 7c). The above results demonstrated the possibility of in vivo synergistic starvation/PTT/HAP therapy based on PDA–PVAMBs@GOx–TPZ.

After different treatments, the tumor volume on each mouse was measured every two days using a caliper (Fig. 7d). The mice tumor sizes of PDA–PVAMBs@GOx group showed a slight decrease compared with the PBS control group, suggested the limitation of starvation therapy. In contrast, the groups of PDA–PVAMBs@GOx + Laser and PDA–PVAMBs@GOx–TPZ had improved antitumor effects. The most effective tumor therapy was found for the triple synergistic treatment group of PDA–PVAMBs@GOx–TPZ + Laser during the treatment course of 14 days. This was further confirmed by the photographs and weights of tumors exercised from tumor-bearing mice (Fig. 7e and 7f). The body weights of the mice during the 14-day treatment were recorded and there was no significant difference among different groups (Fig. 7g). After various treatments at day 14, both H&E and terminal deoxynucleotidyl transferase dUTP nick end labeling (TUNEL) staining of tumors were then carried out to further examine the synergistic treatment effects (Fig. 7h). The results showed that the largest cell destruction and apoptosis degree was observed in the PDA–PVAMBs@GOx–TPZ + Laser group. Additionally, after 14 days of treatment, hearts, livers, spleens, lungs, and kidneys of the sacrificed mice were sectioned and analyzed by H&E staining. The results showed that there was no significant pathological change of organs of the triple synergistic therapy of PDA–PVAMBs@GOx–TPZ + Laser (Fig. S10), demonstrating the low systemic toxicity. The above results demonstrated that the prepared therapeutic platform could achieve an excellent synergistic therapy effect with no obvious systemic side effects.

In this study, intratumoral injection was chosen to deliver the therapeutic reagents into tumors. Several studies have shown that the production of H_2O_2 and the decrease of glucose due to GOx reaction in intravenous administration may cause adverse reactions to normal tissues and the intratumoral injection could be a better delivery approach for GOx-based agents to minimize side effects.[43-45] In practice, the application of intratumoral injection is limited by the challenge to reach deep tissues and our therapeutic system can mainly be used for superficial tumors. Compared with nanosized platforms, microsized platforms could prolong the tumor retention time for effective long-term therapy.[46]

4. Conclusion

In summary, a theranostic hybrid microbubble platform based on PDA–PVAMBs@GOx–TPZ was designed for dual-modality US/enhanced PA imaging-guided synergistic starvation, low-temperature PTT, and hypoxia-activated therapy with long-term tumor retention and minimum systemic side effects. It was found that integration PDA with MBs enhanced the PA contrast by approximately 6.5-fold relative to the free dispersed PDA NPs with a superior PA signal stability. After PDA–PVAMBs@GOx injection, O_2 inside PDA–PVAMBs was firstly released to promote starvation therapy by loaded GOx. Next, the enzymatic activity of GOx could be enhanced by low-temperature PTT at an optimal temperature around 47 ℃ for an upgraded starvation therapy. Afterward, the generated hypoxia during GOx reaction activated hypoxia-prodrug TPZ to generate a sequential and synergistic therapeutic effect. Both *in vitro* and *in vivo* results showed that the triple synergistic therapy significantly inhibited the growth of tumors and achieved maximum therapeutic effects. Through US/PA imaging monitoring, PDA–PVAMBs @ GOx could be retained for about 7 days and gradually degrade to achieve long-term treatment. Moreover, the good hemocompatibility and low toxicity to organs of this theranostic platform ensured systemic biosafety. This unique platform could provide a new approach for imaging-guided combinational therapy with high therapeutic efficiency and minimum adverse effects.

Author Contributions

F. Tian designed the study and prepared the manuscript. F. Tian, X.J. Zhong, J.K. Zhao, Y.T. Gu, Y.D. Fan and F. Shi performed the experiments and collected the data. Y. Zhang, Y. H. Tan and W. Chen interpreted the data. M. Yang provided experiment guidance and revised the manuscript.

Conflicts of interest

There are no conflicts to declare.

Acknowledgements

This work was supported by the National Natural Science Foundation of China (NSFC) (Grant No. 31771077), the Hong Kong Research Council Collaborative Research Grant (C5011-19G), Innovation and Technology Fund, Guangdong- Hong Kong Cooperation Scheme (GHP-039-18GD), the Hong Kong Research Council General Research Fund (PolyU 15216917) and the Hong Kong Polytechnic University Internal Fund (1-ZE1E).

References

1 P. Gotwals, S. Cameron, D. Cipolletta, V. Cremasco, A. Crystal, B. Hewes, B. Mueller, S. Quaratino, C. Sabatos-Peyton, L. Petruzzelli, J. A. Engelman and G. Dranoff, *Nat. Rev. Cancer*, 2017, **17**, 286–301.

2 R. B. Mokhtari, T. S. Homayouni, N. Baluch, E. Morgatskaya, S. Kumar, B. Das and H. Yeger, *Oncotarget*, 2017, **8**, 38022–38043.
3 T. C. Chou, *Cancer Res*, 2010, **70**, 440–446.
4 M. G. Vander Heiden, L. C. Cantley and C. B. Thompson, *Science*, 2009, **324**, 1029–1033.
5 S. Yu, Z. Chen, X. Zeng, X. Chen and Z. Gu, *Theranostics*, 2019, **9**, 8026–8047.
6 M. Wang, D. Wang, Q. Chen, C. Li, Z. Li, J. Lin, *Small*, 2019, **15**, 1903895.
7 L. H. Fu, C. Qi, Y. R. Hu, J. Lin and P. Huang, *Adv. Mater.*, 2019, **31**, 1808325.
8 L. Shan, W. Fan, W. Wang, W. Tang, Z. Yang, Z. Wang, Y. Liu, Z. Shen, Y. Dai and S. Cheng, *ACS Nano*, 2019, **13**, 8903–8916.
9 J. Zhou, M. Li, Y. Hou, Z. Luo, Q. Chen, H. Cao, R. Huo, C. Xue, L. Sutrisno, L. Hao, Y. Cao, H. Ran, L. Lu, K. Li and K. Cai, *ACS Nano*, 2018, **12**, 2858–2872.
10 L. Zhang, Z. Wang, Y. Zhang, F. Cao, K. Dong, J. Ren and X. Qu, *ACS Nano*, 2018, **12**, 10201–10211.
11 Y. Guo, H. R. Jia, X. Zhang, X. Zhang, Q. Sun, S. Z. Wang, J. Zhao and F. G. Wu, *Small*, 2020, **16**, 2000897.
12 C. Yang, M. R. Younis, J. Zhang, J. L. Qu, J. Lin and P. Huang, *Small*, 2020, **16**, 2001518.
13 S. B. Bankar, M. V. Bule, R. S. Singhal and L. Ananthanarayan, *Biotechnol. Adv.*, 2009, **27**, 489–501.
14 L. Zhang, Y. Fan, Z. Yang, M. Yang, C.Y. Wong, *Journal of nanobiotechnology,* 2021*,* **19**, 1-16.
15 Y. Zhang, W. Qiu, M. Zhang, L. Zhang and X. Zhang, *ACS Appl. Mater. Interfaces*, 2018, **10**, 15030–15039.
16 R. M. Phillips, *Cancer Chemother. Pharmacol.*, 2016, **77**, 441–457.
17 W. A. Denny, *Lancet Oncol.*, 2000, **1**, 25–29.
18 J. J. Hu, M. D. Liu, F. Gao, Y. Chen, S. Y. Peng, Z. H. Li, H. Cheng and X. Z. Zhang, *Biomaterials*, 2019, **217**, 119303.
19 X. Huang and M. A. El-Sayed, *Alexandria Med. J.*, 2011, **47**, 1–9.
20 L. Zou, H. Wang, B. He, L. Zeng, T. Tan, H. Cao, X. He, Z. Zhang, S. Guo and Y. Li, *Theranostics*, 2016, **6**, 762–772.
21 G. Gao, Y. W. Jiang, Y. Guo, H. R. Jia, X. Cheng, Y. Deng, X. W. Yu, Y. X. Zhu, H. Y. Guo, W. Sun, X. Y. Liu, J. Zhao, S. H. Yang, Z. W. Yu, F. M. S. Raya, G. L. Liang and X. Liu, *Adv. Funct. Mater.*, 2020, **30**, 1909391.
22 L. Zhou, J. Zhao, Y. Chen, Y. Zheng, J. Li, J. Zhao, J. Zhang, Y. Liu, X. Liu and S. Wang, *Colloids Surf., B*, 2020, **195**, 111243.
23 X. Su, C. Chan, J. Shi, M.K. Tsang, Y. Pan, C. Cheng, O. Gerile and M. Yang, *Biosens. Bioelectron.* 2017, **92**, 489-495
24 X. Li, J. Kim, J. Yoon and X. Chen, *Adv. Mater.*, 2017, **29**, 1606857.
25 Y. Liu, P. Bhattarai, Z. Dai and X. Chen, *Chem. Soc. Rev.*, 2019, **48**, 2053–2108.
26 E. J. Swanson, V. Mohan, J. Kheir and M. A. Borden, *Langmuir*, 2010, **26**, 15726–15729.
27 J. A. Feshitan, N. D. Legband, M. A. Borden, B. S. Terry, *Biomaterials*, 2014, **35**, 2600–2606.
28 M.T. Au, J. Shi, Y. Fan, J. Ni, C. Wen, M. Yang, *ACS Nano, 2021,* **15**, 11711-11723
29 Y. Liu, K. Ai and L. Lu, *Chem. Rev.*, 2014, **114**, 5057–5115.
30 B. Poinard, S. Z. Y. Neo, E. L. L. Yeo, H. P. S. Heng, K. G. Neoh and J. C. Y. Kah, *ACS Appl. Mater. Interfaces*, 2018, **10**, 21125–21136.
31 Y. Liu, K. Ai, J. Liu, M. Deng, Y. He and L. Lu, *Adv. Mater.*, 2013, **25**, 1353–1359.
32 A. J. Dixon, S. Hu, A. L. Klibanov, J. A. Hossack, *Small*, 2015, **11**, 3066–3077.
33 J. D. Dove, M. A. Borden and T. W. Murray, *Opt. Lett.*, 2014, **39**, 3732–3735.
34 K. Firouzi, E. Stride and N. Saffari, *J. Acoust. Soc. Am.*, 2013, **133**, 3853–3862.
35 Y. Toumia, F. Domenici, S. Orlanducci, F. Mura, D. Grishenkov, P. Trochet, S. Lacerenza, F. Bordi and G. Paradossi, *ACS Appl. Mater. Interfaces*, 2016, **8**, 16465–16475.
36 J. Ren, L. Zhang, J. Zhang, W. Zhang, Y. Cao, Z. Xu, H. Cui, Y. Kang and P. Xue, *Biomaterials*, 2020, **234**, 119771.
37 R. C. Bakker, M. G. E. H. Lam, S. A. van Nimwegen, A. J. W. P. Rosenberg, R. J. J. van Es and J. F. W. Nijsen, *J. Radiol. Oncol.*, 2017, **6**, 323–341.
38 E. Huynh, B. Y. Leung, B. L. Helfield, M. Shakiba, J. A. Gandier, C. S. Jin, E. R. Master, B. C. Wilson, D. E. Goertz and G. Zheng, *Nat. Nanotechnol.*, 2015, **10**, 325–332.
39 E. Stride and N. Saffari, *Proc. Inst. Mech. Eng., Part H*, 2003, **217**, 429–447.
40 M. O. Culjat, D. Goldenberg, P. Tewari and R. S. Singh, *Ultrasound Med. Biol.*, 2010, **36**, 861–873.
41 C. M. Pitsillides, E. K. Joe, X. Wei, R. R. Anderson and C. P. Lin, *Biophys. J.*, 2003, **84**, 4023–4032.
42 N. Zeng and A. B. Murphy, *Nanotechnology*, 2009, **20**, 375702.
43 L. H. Fu, Y. R. Hu, C. Qi, T. He, S. Jiang, C. Jiang, J. He, J. Qu, J. Lin and P. Huang, *ACS Nano*, 2019, **13**, 13985–13994.
44 W. Zhao, J. Hu and W. Gao, *ACS Appl. Mater. Interfaces*, 2017, **9**, 23528–23535.
45 Y. Zhang, Y. Yang, S. Jiang, F. Li, J. Lin, T. Wang and P. Huang, *Mater. Horiz.*, 2019, **6**, 169–175.
46 X. Lu, L. Miao, W. Gao, Z. Chen, K. J. McHugh, Y. Sun, Z. Tochka, S. Tomasic, K. Sadtler, A. Hyacinthe, Y. Huang, T. Graf, Q. Hu, M. Sarmadi, R. Langer, D. G. Anderson and A. Jaklenec, *Sci. Transl. Med.*, 2020, **12**, eaaz6606.